

SPD domain-specific batch normalization to crack interpretable unsupervised domain adaptation in EEG

Reinmar J. Kobler^{1,2}, Jun-ichiro Hirayama¹, Qibin Zhao¹, Motoaki Kawanabe^{1,2}

¹RIKEN Center for Advanced Intelligence Project (RIKEN AIP), Tokyo, Japan

²Advanced Telecommunications Research Institute International (ATR), Kyoto, Japan

{reinmar.kobler, qibin.zhao}@riken.jp

jun-ichiro.hirayama@a.riken.jp, kawanabe@atr.jp

Abstract

Electroencephalography (EEG) provides access to neuronal dynamics non-invasively with millisecond resolution, rendering it a viable method in neuroscience and healthcare. However, its utility is limited as current EEG technology does not generalize well across domains (i.e., sessions and subjects) without expensive supervised re-calibration. Contemporary methods cast this transfer learning (TL) problem as a multi-source/-target unsupervised domain adaptation (UDA) problem and address it with deep learning or shallow, Riemannian geometry aware alignment methods. Both directions have, so far, failed to consistently close the performance gap to state-of-the-art domain-specific methods based on tangent space mapping (TSM) on the symmetric positive definite (SPD) manifold. Here, we propose a theory-based machine learning framework that enables, for the first time, learning domain-invariant TSM models in an end-to-end fashion. To achieve this, we propose a new building block for geometric deep learning, which we denote SPD domain-specific momentum batch normalization (SPDDSMBN). A SPDDSMBN layer can transform domain-specific SPD inputs into domain-invariant SPD outputs, and can be readily applied to multi-source/-target and online UDA scenarios. In extensive experiments with 6 diverse EEG brain-computer interface (BCI) datasets, we obtain state-of-the-art performance in inter-session and -subject TL with a simple, intrinsically interpretable network architecture, which we denote TSMNet.

1 Introduction

Electroencephalography (EEG) measures multi-channel electric brain activity from the human scalp with millisecond precision [1]. Transient modulations in the rhythmic brain activity can reveal cognitive processes [2], affective states [3] and a persons health status [4]. Unfortunately, these modulations exhibit low signal-to-noise ratio (SNR), domain shifts (i.e., changes in the data distribution) and have low specificity, rendering statistical learning a challenging task - particularly in the context of brain-computer interfaces (BCI) [5] where the goal is to predict a target from a short segment of multi-channel EEG data in real-time.

Under domain shifts, domain adaptation (DA), defined as learning a model from a source domain that performs well on a related target domain, offers principled statistical learning approaches with theoretical guarantees [6, 7]. DA in the BCI field mainly distinguishes inter-session and -subject transfer learning (TL) [8]. In inter-session TL, domain shifts, are expected across sessions mainly due to mental drifts (low specificity) as well as differences in the relative positioning of the electrodes and their impedances. Inter-subject TL is more difficult, as domain shifts are additionally driven by structural and functional differences in brain networks as well as variations in the performed task [9].

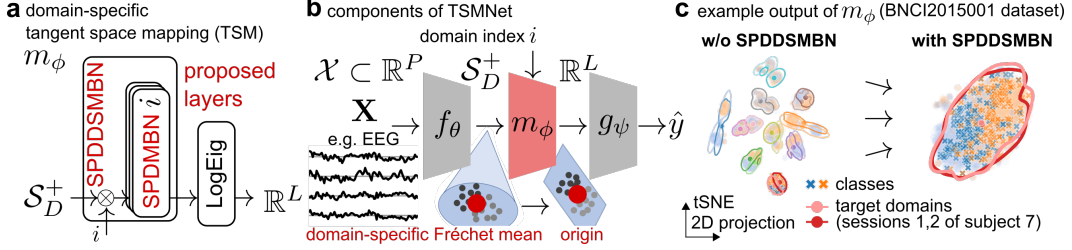


Figure 1: Visualization of the proposed framework around SPD domain-specific momentum batch normalization (SPDDSMBN) (a) that learns parameters $\Theta = \{\theta, \phi, \psi\}$ of typical tangent space mapping (TSM) models (b) *end-to-end* to crack multi-source/-target unsupervised domain adaptation (MSMTUDA) on S_D^+ for EEG data (c, illustrative example). For EEG data, we propose a simple, intrinsically interpretable parametrization of f and g , denoted TSMNet, and obtain SOA performance.

These domain shifts are traditionally circumvented by recording labeled calibration data and fitting domain-specific models [10, 11]. As recording calibration data is costly, models that are robust to scarce data with low SNR perform well in practice. Currently, tangent space mapping (TSM) models [12, 13] operating with symmetric, positive definite (SPD) covariance descriptors of preprocessed data are considered state-of-the-art (SOA) [10, 14, 15]. They are well suited for EEG data as they exhibit invariances to linear mixing of latent sources [16], and are consistent [13] and intrinsically interpretable [17] estimators for generative models that encode label information with a log-linear relationship in source power modulations.

Competitive, supervised calibration-free methods are one of the long-lasting grand challenges in EEG neurotechnology research [5, 10, 18, 19, 15]. Among the applied transfer learning techniques, including multi-task learning [20] and domain-invariant learning [21–23], unsupervised domain adaptation (UDA) [24] is considered as key to overcome this challenge [10, 19]. Contemporary methods cast the problem as a multiple source and target UDA problem and address it with deep learning [25–28] or shallow, Riemannian geometry aware alignment methods [29–32]. Successful methods must cope with notoriously small and heterogeneous datasets (i.e., dozens of domains with a few dozens observations per domain and class). In a recent, relatively large scale inter-subject and -dataset TL competition with few labeled examples per target domain [19], deep learning approaches that aligned the first and second order statistics either in input [33, 27] or latent space [34] obtained the highest scores. Whereas, in a pure UDA competition [15] with a smaller dataset, Riemannian geometry aware approaches dominated. With the increasing popularity of geometric deep learning [35], Ju and Guan [36] proposed a architecture based on SPD neural networks [37] to align SPD features in latent space and attained similar scores as convolutional neural nets. Despite the tremendous advances in recent years, the field still lacks methods that can consistently close the performance gap to state-of-the-art domain-specific methods.

To close this gap, we propose a theory-based machine learning framework around domain-specific batch normalization on the SPD manifold (Figure 1). We first extend momentum batch normalization (MBN) [32] to SPDMBN that controls the Fréchet mean and variance of SPD data. In a theoretical analysis, we show under reasonable assumptions that SPDMBN can track and converge to the data’s true Fréchet mean, enabling, for the first time, end-to-end learning of feature extractors, TSM and tangent space classifiers. Building upon this insight, we combine SPDMBN with domain-specific batch normalization (DSBN) [38] to form SPDDSMBN. A SPDDSMBN layer can transform domain-specific SPD inputs into domain-invariant SPD outputs. Like DSBN, SPDDSMBN easily extends to multi-source, multi-target and online UDA scenarios. Ultimately, the proposed methods are combined in a simple, intrinsically interpretable network architecture, denoted TSMNet. We obtain state-of-the-art performance in inter-session and -subject UDA on small and large scale EEG BCI datasets, and show in an ablation study that the performance increase is driven by performing DSBN on the SPD manifold.

2 Preliminaries

Multi-source multi-target unsupervised domain adaptation (MSMTUDA) Let \mathcal{X} denote the space of input features, \mathcal{Y} a label space, and $\mathcal{I}_d \subset \mathbb{N}$ an index set that contains unique domain identifiers. In the multi-source, multi-target unsupervised domain adaptation scenario considered here, we are given a set $\mathcal{T}^{source} = \{\mathcal{T}_i | i \in \mathcal{I}_d^{source} \subset \mathcal{I}_d\}$ with $|\mathcal{I}_d^{source}| = N$ domains. Each

domain $\mathcal{T}_i = \{(\mathbf{X}_{ij}, y_{ij})\}_{j=1}^M \sim P_{XY}^i$ contains M observations of feature ($\mathbf{X} \in \mathcal{X}$) and label ($y \in \mathcal{Y}$) tuples sampled from a joint distribution P_{XY}^i .¹ While the joint distributions can be different (but related) across domains, we assume that the class priors are the same (i.e., $P_Y^i = P_Y$). The goal is to learn a predictive function $h : \mathcal{X} \times \mathcal{I}_d \rightarrow \mathcal{Y}$ that, once fitted to \mathcal{T}^{source} , can generalize to unseen target domains $\mathcal{T}^{target} = \{\mathcal{T}_l | l \in \mathcal{I}_d^{target} \subset \mathcal{I}_d, \mathcal{I}_d^{target} \cap \mathcal{I}_d^{source} = \emptyset\}$ merely based on *unsupervised* adaptation of h to each target domain \mathcal{T}_l once its label l and features $\{\mathbf{X}_{il}\}_{j=1}^M \sim P_X^l$ are revealed.

Riemannian geometry on \mathcal{S}_D^+ We start with recalling notions of geometry on the space of real $D \times D$ symmetric positive definite (SPD) matrices $\mathcal{S}_D^+ = \{\mathbf{Z} \in \mathbb{R}^{D \times D} : \mathbf{Z}^T = \mathbf{Z}, \mathbf{Z} \succ 0\}$. The space \mathcal{S}_D^+ forms a cone shaped Riemannian manifold in $\mathbb{R}^{D \times D}$ [39]. A Riemannian manifold \mathcal{M} is a smooth manifold equipped with an inner product on the tangent space $\mathcal{T}_{\mathbf{Z}}\mathcal{M}$ at each point $\mathbf{Z} \in \mathcal{M}$. Tangent spaces have Euclidean structure with easy to compute distances $\mathcal{T}_{\mathbf{Z}}\mathcal{M} \times \mathcal{T}_{\mathbf{Z}}\mathcal{M} \rightarrow \mathbb{R}^+$ which locally approximate Riemannian distances on \mathcal{M} induced by an inner product [40]. Logarithmic $\text{Log}_{\mathbf{Z}} : \mathcal{M} \rightarrow \mathcal{T}_{\mathbf{Z}}\mathcal{M}$ and exponential $\text{Exp}_{\mathbf{Z}} : \mathcal{T}_{\mathbf{Z}}\mathcal{M} \rightarrow \mathcal{M}$ mappings project points to and from tangent spaces.

Equipping \mathcal{S}_D^+ with the inner product $\langle \mathbf{S}_1, \mathbf{S}_2 \rangle_{\mathbf{Z}} = \|\mathbf{Z}^{-1}\mathbf{S}_1\mathbf{Z}^{-1}\mathbf{S}_2\|_F$ for points $\mathbf{S}_1, \mathbf{S}_2$ in the tangent space $\mathcal{T}_{\mathbf{Z}}\mathcal{S}_D^+$ (i.e., the space of real symmetric $D \times D$ matrices) results in a globally defined affine invariant Riemannian metric (AIRM) on \mathcal{S}_D^+ [41, 39], which can be computed in closed form:

$$\delta_{AIRM}(\mathbf{Z}_1, \mathbf{Z}_2) = \|\log(\mathbf{Z}_1^{-\frac{1}{2}}\mathbf{Z}_2\mathbf{Z}_1^{-\frac{1}{2}})\|_F \quad (1)$$

where \mathbf{Z}_1 and \mathbf{Z}_2 are two SPD matrices, $\log(\cdot)$ denotes the matrix logarithm², $\|\cdot\|_F$ the Frobenius norm. Due to affine invariance, we have $\delta_{AIRM}(\mathbf{A}\mathbf{Z}_1\mathbf{A}^T, \mathbf{A}\mathbf{Z}_2\mathbf{A}^T) = \delta_{AIRM}(\mathbf{Z}_1, \mathbf{Z}_2)$ for any invertible affine transformation matrix \mathbf{A} . The exponential and logarithmic mapping are also globally defined in closed form as

$$\text{Log}_{\mathbf{Z}}(\mathbf{Z}) = \mathbf{Z}^{\frac{1}{2}}\log(\mathbf{Z}^{-\frac{1}{2}}\mathbf{Z}\mathbf{Z}^{-\frac{1}{2}})\mathbf{Z}^{\frac{1}{2}} \quad (2)$$

$$\text{Exp}_{\mathbf{Z}}(\mathbf{S}) = \mathbf{Z}^{\frac{1}{2}}\exp(\mathbf{Z}^{-\frac{1}{2}}\mathbf{S}\mathbf{Z}^{-\frac{1}{2}})\mathbf{Z}^{\frac{1}{2}} \quad (3)$$

For a set of SPD points $\mathcal{Z} = \{\mathbf{Z}_j \in \mathcal{S}_D^+\}_{j \leq M}$, we will use the notion of Fréchet mean $\mathbf{G} \in \mathcal{S}_D^+$ and Fréchet variance $\nu^2 \in \mathbb{R}^+$. The Fréchet mean \mathbf{G} is defined as the minimizer of the average squared distances

$$\mathbf{G} = \text{FM}(\mathcal{Z}) = \arg \min_{\mathbf{P} \in \mathcal{S}_D^+} \frac{1}{M} \sum_{j=1}^M \delta_{AIRM}^2(\mathbf{P}, \mathbf{Z}_j) \quad (4)$$

For $M = 2$, there is a closed form solution expressed as

$$\text{FM}(\{\mathbf{Z}_1, \mathbf{Z}_2\}; \gamma) = \mathbf{Z}_1 \#_{\gamma} \mathbf{Z}_2 = \mathbf{Z}_1^{\frac{1}{2}} \left(\mathbf{Z}_1^{-\frac{1}{2}} \mathbf{Z}_2 \mathbf{Z}_1^{-\frac{1}{2}} \right)^{\gamma} \mathbf{Z}_1^{\frac{1}{2}} \quad (5)$$

with weight $\gamma = 0.5$. Choosing $\gamma \in [0, 1]$ computes weighted means along the geodesic (i.e., the shortest curve) that connects both points. For $M > 2$, (4) can be solved using the Karcher flow algorithm [42], which iterates between projecting the data to the tangent space (2) at the current estimate, arithmetic averaging, and projecting the result back (3) to obtain a new estimate. The Fréchet variance ν^2 is defined as the attained value at the minimizer \mathbf{G}

$$\nu^2 = \text{FV}(\mathcal{Z}) = \text{Var}_{\mathbf{G}}(\mathcal{Z}) = \frac{1}{M} \sum_{j=1}^M \delta_{AIRM}^2(\mathbf{G}, \mathbf{Z}_j) \quad (6)$$

3 Domain-specific batch normalization on \mathcal{S}_D^+

In this section, we briefly review batch normalization (BN) [43] variants with a focus on \mathcal{S}_D^+ as well as domain-specific batch normalization (DSBN) [38]. We then present SPDDSBM and show in a theoretical analysis that the running estimates converge to the true domain-specific Fréchet means under reasonable assumptions.

¹For ease of notation, although not required by our method, we assume that M is the same for each domain.

²For SPD matrices, powers, logarithms and exponentials can be computed via eigen decomposition.

Batch normalization Batch normalization (BN) [43] is a widely used training technique in deep learning as BN layers speed up convergence and improve generalization via smoothing of the energy landscape [44, 32]. A standard BN layer applies slightly different transformations during training and testing to independent and identically distributed (iid) observations $\mathbf{x}_j \in \mathbb{R}^d$ within a minibatch \mathcal{B} of size M drawn from a dataset \mathcal{T} . During training, the data are whitened using the batch mean $\mathbf{g}_{\mathcal{B}} \in \mathbb{R}^d$ and variance $\mathbf{s}_{\mathcal{B}}^2 \in \mathbb{R}_+^d$, and then scaled and shifted to have a parametrized mean \mathbf{g}_{ϕ} and variance \mathbf{s}_{ϕ}^2 . The BN layer input output relation is expressed as

$$\text{BN}(\mathbf{x}_j; \mathbf{g}_{\phi}, \mathbf{s}_{\phi}, \varepsilon, \gamma) = \mathbf{s}_{\phi} \oslash (\mathbf{s}_{\mathcal{B}} + \varepsilon \mathbf{1}_d) \odot (\mathbf{x} - \mathbf{g}_{\mathcal{B}}) + \mathbf{g}_{\phi}, \quad \forall \mathbf{x}_j \in \mathcal{B} \quad (7)$$

where the operators \odot and \oslash perform element-wise multiplication and division, $\varepsilon \in \mathbb{R}_+$ is a small stabilizing constant, and γ a momentum parameter that is used internally to update running estimates of the dataset's statistics $(\mathbf{g}_{\mathcal{T}}, \mathbf{s}_{\mathcal{T}}^2)$; they are used in (7) during testing.

Using batch statistics to whiten observations during training rather than running estimates introduces noise whose level depends on the batch size [32]; smaller batch sizes raise the noise level. The introduced noise regularizes the training process, which can help to escape poor local minima in initial learning but also lead to underfitting. Momentum BN (MBN) [32] allows small batch sizes while avoiding underfitting. Like batch renormalization (BreN) [45], MBN uses running estimates in (7) during training and testing. The key difference is that MBN keeps two sets of running statistics; one for training and one for testing. The latter are updated conventionally, while the former are updated with momentum parameter $\gamma_{\text{train}}(k)$ that decays over training steps k . MBN can, therefore, quickly escape poor local minima during initial learning and avoid underfitting at later stages [32].

Batch normalization on \mathcal{S}_D^+ It is intractable to compute the Fréchet mean $\mathbf{G}_{\mathcal{B}}$ and variance $\nu_{\mathcal{B}}^2$ for each minibatch $\mathcal{B} = \{\mathbf{Z}_j \in \mathcal{S}_D^+\}_{j=1}^M$, as there is no efficient algorithm to solve (4). Brooks et al. [46] proposed Riemannian Batch Normalization (RBN) as a tractable approximation. RBN approximately solves (4) by aborting the iterative Karcher flow algorithm after one iteration. To transform $\mathbf{Z}_j \in \mathcal{B}$ with estimated mean $\hat{\mathbf{G}}_{\mathcal{B}}$ to vary around \mathbf{G}_{ϕ} , parallel transport can be used [47, 31, 46].³ The RBN input output transformation is then expressed as

$$\text{RBN}(\mathbf{Z}_j; \mathbf{G}_{\phi}, \gamma) = \Gamma_{\hat{\mathbf{G}}_{\mathcal{B}} \rightarrow \mathbf{G}_{\phi}}(\mathbf{Z}_j) = \mathbf{E}^T \mathbf{Z}_j \mathbf{E}, \quad \mathbf{E} = (\hat{\mathbf{G}}_{\mathcal{B}}^{-1} \mathbf{G}_{\phi})^{\frac{1}{2}}, \quad \forall \mathbf{Z}_j \in \mathcal{B} \quad (8)$$

Using (5), the running estimate of the dataset's Fréchet mean can be computed in closed form

$$\mathbf{G}_{\mathcal{T}}(k) = \mathbf{G}_{\mathcal{T}}(k-1) \#_{\gamma} \hat{\mathbf{G}}_{\mathcal{B}} \quad (9)$$

Kobler et al. [48] proposed an extension to RBN, denoted SPD batch renormalization (SPDBN) that controls both Fréchet mean and variance. Like BreN, SPDBN uses running estimates $\mathbf{G}_{\mathcal{T}}(k)$ and $\nu_{\mathcal{T}}(k)$ during training and testing. To transform $\mathbf{Z}_j \in \mathcal{B}$ to vary around \mathbf{G}_{ϕ} with variance ν_{ϕ}^2 , each observation is first transported to vary around the identity matrix \mathbf{I} , rescaled via computing matrix powers and finally transported to vary around \mathbf{G}_{ϕ} . The sequence of operations can be expressed as

$$\text{SPDBN}(\mathbf{Z}_j; \mathbf{G}_{\phi}, \nu_{\phi}^2, \varepsilon, \gamma) = \Gamma_{\mathbf{I} \rightarrow \mathbf{G}_{\phi}} \circ \Gamma_{\mathbf{G}_{\mathcal{T}}(k) \rightarrow \mathbf{I}}(\mathbf{Z}_j)^{\frac{\nu_{\phi}}{\nu_{\mathcal{T}}(k) + \varepsilon}}, \quad \forall \mathbf{Z}_j \in \mathcal{B} \quad (10)$$

The standard backpropagation framework with extensions for structured matrices [49] and manifold-constrained gradients [40] can be used to propagate gradients through RBN and SPDBN layers and learn the parameters $(\mathbf{G}_{\phi}, \nu_{\phi})$.

Domain-specific batch normalization on \mathcal{S}_D^+ Considering a MSUDA scenario, Chang et al. [38] proposed a domain-specific BN (DSBN) layer which simply keeps multiple parallel BN layers and distributes observations according to the associated domains. Formally, we consider minibatches \mathcal{B} that form the union of $N_{\mathcal{B}} \leq |\mathcal{I}_d|$ domain-specific minibatches \mathcal{B}_i drawn from distinct domains $i \in \mathcal{I}_{\mathcal{B}} \subseteq \mathcal{I}_d$. As before, each \mathcal{B}_i contains $j = 1, \dots, M/N_{\mathcal{B}}$ iid observations \mathbf{x}_j . A DSBN layer mapping $\mathbb{R}^d \times \mathcal{I}_d \rightarrow \mathbb{R}^d$ can then be expressed as

$$\text{DSBN}(\mathbf{x}_j, i) = \text{BN}_i(\mathbf{x}_j; \mathbf{g}_{\phi_i}, \mathbf{s}_{\phi_i}, \varepsilon, \gamma), \quad \forall \mathbf{x}_j \in \mathcal{B}_i, \quad \forall i \in \mathcal{I}_{\mathcal{B}} \quad (11)$$

In practice, the batch size M is typically fixed. The particular choice is influenced by resource availability and the desired noise level introduced by minibatch based stochastic gradient descent. A drawback of DSBN is that for a fixed batch size M and an increasing number of source domains $N_{\mathcal{B}}$,

³On \mathcal{S}_D^+ parallel transport can be used to transport points on the tangent space and manifold.

Algorithm 1: SPD momentum batch normalization (SPDMBN)

Input : batch $\mathcal{B} = \{\mathbf{Z}_j \in \mathcal{S}_D^+ \}_{j=1}^M$ at training step k ,
running mean $\bar{\mathbf{G}}_{\mathcal{T}}(k-1)$, $\bar{\mathbf{G}}_{\mathcal{T}}(0) = \mathbf{I}$ and variance $\bar{\nu}_{\mathcal{T}}^2(k-1)$, $\bar{\nu}_{\mathcal{T}}(0) = 1$ for training,
running mean $\tilde{\mathbf{G}}_{\mathcal{T}}(k-1)$, $\tilde{\mathbf{G}}_{\mathcal{T}}(0) = \mathbf{I}$ and variance $\tilde{\nu}_{\mathcal{T}}^2(k-1)$, $\tilde{\nu}_{\mathcal{T}}(0) = 1$ for testing,
learnable parameters $(\mathbf{G}_{\phi}, \nu_{\phi})$, and momentum for training and testing $\gamma_{train}(k), \gamma \in [0, 1]$

Output : normalized batch $\{\tilde{\mathbf{Z}}_j = \text{SPDMBN}(\mathbf{Z}_j) \in \mathcal{S}_D^+ \mid \mathbf{Z}_j \in \mathcal{B}\}$

if training then
 $\hat{\mathbf{G}}_{\mathcal{B}} = \text{karcher_flow}(\mathcal{B}, \text{steps} = 1);$ // approx. solve problem (4)
 $\bar{\mathbf{G}}_{\mathcal{T}}(k) = \bar{\mathbf{G}}_{\mathcal{T}}(k-1) \#_{\gamma_{train}(k)} \hat{\mathbf{G}}_{\mathcal{B}};$ // update running stats for training
 $\bar{\nu}_{\mathcal{T}}^2(k) = (1 - \gamma_{train}(k))\bar{\nu}_{\mathcal{T}}^2(k-1) + \gamma_{train}(k)\text{Var}_{\bar{\mathbf{G}}_{\mathcal{T}}(k)}(\mathcal{B})$
 $\tilde{\mathbf{G}}_{\mathcal{T}}(k) = \tilde{\mathbf{G}}_{\mathcal{T}}(k-1) \#_{\gamma} \hat{\mathbf{G}}_{\mathcal{B}};$ // update running stats for testing
 $\tilde{\nu}_{\mathcal{T}}^2(k) = (1 - \gamma)\tilde{\nu}_{\mathcal{T}}^2(k-1) + \gamma\text{Var}_{\tilde{\mathbf{G}}_{\mathcal{T}}(k)}(\mathcal{B})$
end

$(\mathbf{G}_{\mathcal{T}}(k), \nu_{\mathcal{T}}^2(k)) = (\bar{\mathbf{G}}_{\mathcal{T}}(k), \bar{\nu}_{\mathcal{T}}(k))$ **if training else** $(\tilde{\mathbf{G}}_{\mathcal{T}}(k), \tilde{\nu}_{\mathcal{T}}(k))$
 $\tilde{\mathbf{Z}}_j = \Gamma_{\mathbf{I} \rightarrow \mathbf{G}_{\phi}} \circ \Gamma_{\mathbf{G}_{\mathcal{T}}(k) \rightarrow \mathbf{I}}(\mathbf{Z}_j)^{\frac{\nu_{\phi}}{\nu_{\mathcal{T}}(k) + \varepsilon}};$ // use (10) to whiten, rescale and rebias

the effective batch size declines for the BN layers within DSBN. Since small batch sizes increase the noise level introduced by BN, increasing the number of domains per batch can lead to underfitting [32].

Domain-specific batch normalization could be extended to \mathcal{S}_D^+ by replacing BN in (11) with RBN or SPDBN. However, we believe that the performance can be improved by extending MBN to the SPD manifold. We list the pseudocode of our proposed extension, which we denote SPDMBN, in algorithm 1. As MBN [32], we decay $\gamma_{train}(k)$ with a clamped exponential decay schedule

$$\gamma_{train}(k) = 1 - \gamma_{min}^{\frac{1}{K-1} \max(K-k, 0)} + \gamma_{min} \quad (12)$$

where K defines the training step at which $\gamma_{min} \in [0, 1]$ should be attained. The proposed layer is then formally defined as

$$\text{SPDDSMBN}(\mathbf{Z}_j, i) = \text{SPDMBN}_i(\mathbf{Z}_j; \mathbf{G}_{\phi_i}, \nu_{\phi_i}, \varepsilon, \gamma, \gamma_{train}(k)), \forall \mathbf{Z}_j \in \mathcal{B}_i \subset \mathcal{S}_D^+, \forall i \in \mathcal{I}_{\mathcal{B}} \quad (13)$$

SPDDSMBN can be readily adapted to new domains, as new SPDMBN layers can be added on the fly. If the entire data of a domain becomes available, the domain-specific Fréchet mean and variance can be estimated by solving (4), otherwise, the update rules in algorithm 1 can be used.

The running mean in SPDMBN converges to the Fréchet mean So far we have introduced SPDMBN which uses approximations of batch-specific Fréchet means to update running estimates of the dataset's Fréchet mean. In the following, we consider models that apply a SPDMBN layer to latent observations generated by a feature extractor $f_{\theta} : \mathcal{X} \rightarrow \mathcal{S}_D^+$ with learnable parameters θ .

We define a dataset containing the latent observations generated with feature set θ_k as $\mathcal{T}_{\theta_k} = \{f_{\theta_k}(\mathbf{x}) \mid \mathbf{x} \in \mathcal{T}\}$, and a minibatch of M iid samples drawn from \mathcal{T}_{θ_k} at training step k as \mathcal{B}_k . We denote the Fréchet mean of \mathcal{T}_{θ_k} as \mathbf{G}_{θ_k} , the Fréchet variance as $\text{Var}_{\theta_k}(\mathcal{T}_{\theta_k})$, and the estimated Fréchet mean, defined in (9), as $\bar{\mathbf{G}}_k$.

Let us assume that the variance of the latent dataset $\mathcal{T}_{\theta_{k-1}}$ at the previous training step with respect to \mathbf{G}_{θ_k} at the current training step is bounded by the current Fréchet variance and the norm of the differences in the parameters

$$\text{Var}_{\theta}(\mathcal{T}_{\theta_{k-1}}) \leq (1 + \|\theta_k - \theta_{k-1}\|) \text{Var}_{\theta}(\mathcal{T}_{\theta_k}) \quad (14)$$

This is, for instance, the case for functions f_{θ} that are smooth in the parameters (i.e., $\exists L > 0 : \delta_{AIRM}(f_{\theta}(\mathbf{x}), f_{\tilde{\theta}}(\mathbf{x})) \leq L\|\theta - \tilde{\theta}\| \forall \mathbf{x} \in \mathcal{T}, \forall \theta, \tilde{\theta}$) and small step sizes.

Proposition 1 (Bound for SPDBN). *Consider the setting defined above, and assumption (14) holds true. Then, the variance $\text{Var}_{\theta}(\bar{\mathbf{G}}_k)$ of the running mean is non-increasing over training steps k if*

$$\|\theta_k - \theta_{k-1}\| \leq \frac{1 - \gamma^2}{(1 - \gamma)^2} - 1 \quad (15)$$

holds true.

The proof is provided in appendix A.1 of the supplementary material and relies on the proof of the geometric law of large numbers [50]. For a fixed $\gamma \in (0, 1)$, Proposition 1 is fulfilled, if the parameter updates are chosen sufficiently small.

Proposition 2 (Convergence of SPDMBN). *If we additionally assume that the parameters θ_k converge to a stationary point θ^* (i.e., $\|\theta_k - \theta^*\| \leq 1/k^\beta$), the momentum parameter is decayed with schedule $\gamma(k) = 1/k^\alpha$, and $\beta > \alpha > 0$, then the running mean \mathbf{G}_k converges to the Fréchet mean \mathbf{G}_{θ^*} in probability as $k \rightarrow \infty$.*

The proof reduces to the proof of the theorem of large numbers on \mathcal{S}_D^+ , provided in [50], since in the limit $k \rightarrow \infty$ the variance introduced by the parameter updates vanishes faster than the variance introduced by the noisy estimates.

SPDMBN to learn tangent space mapping at Fréchet means Typical TSM models for classification [12] and regression [13] first use (2) to project $\mathbf{Z} \in \mathcal{T} \subset \mathcal{S}_D^+$ to the tangent space at the Fréchet mean $\mathbf{G}_{\mathcal{T}}$, then use (8) to transport the result to vary around \mathbf{I} , and finally extract elements in the upper triangular part⁴ to reduce feature redundancy. The invertible mapping $\mathcal{P}_{\mathbf{G}_{\mathcal{T}}} : \mathcal{S}_D^+ \rightarrow \mathbb{R}^{D(D+1)/2}$ is expressed as:

$$\mathcal{P}_{\mathbf{G}_{\mathcal{T}}}(\mathbf{Z}) = \text{upper} \circ \Gamma_{\mathbf{G}_{\mathcal{T}} \rightarrow \mathbf{I}} \circ \text{Log}_{\mathbf{G}_{\mathcal{T}}}(\mathbf{Z}) = \text{upper}(\log(\mathbf{G}_{\mathcal{T}}^{-\frac{1}{2}} \mathbf{Z} \mathbf{G}_{\mathcal{T}}^{-\frac{1}{2}})) \quad (16)$$

We propose to use a SPDMBN layer followed by a LogEig layer [37] to compute a similar mapping m_ϕ (Figure 1a). A LogEig layer simply computes the matrix logarithm and vectorizes the result so that the norm is preserved. If the parametrized mean of SPDMBN is fixed to the identity matrix ($\mathbf{G}_\phi = \mathbf{I}$), the composition computes

$$\begin{aligned} m_\phi(\mathbf{Z}) &= \text{LogEig} \circ \text{SPDMBN}(\mathbf{Z}) = \text{upper} \circ \log \circ \Gamma_{\mathbf{G}_{\mathcal{T}}(k) \rightarrow \mathbf{I}}(\mathbf{Z})^{\frac{\nu_\phi}{\nu_{\mathcal{T}} + \varepsilon}} \\ &= \text{upper} \left(\frac{\nu_\phi}{\nu_{\mathcal{T}}(k) + \varepsilon} \log \left(\mathbf{G}_{\mathcal{T}}^{-\frac{1}{2}}(k) \mathbf{Z} \mathbf{G}_{\mathcal{T}}^{-\frac{1}{2}}(k) \right) \right) \end{aligned} \quad (17)$$

where $(\mathbf{G}_{\mathcal{T}}(k), \nu_{\mathcal{T}}^2(k))$ are the estimated mean and variance at training step k , and $\phi = \{\nu_\phi\}$ the learnable parameters. If the assumptions of proposition 2 are fulfilled, $\mathbf{G}_{\mathcal{T}}(k)$ converges to \mathbf{G} and, in turn, m_ϕ to a scaled version of $\mathcal{P}_{\mathbf{G}}$, since upper is linear.

The mapping m_ϕ offers several advantageous properties. First, the features are projected to a Euclidean vector space where standard layers can be applied and distances are cheap to compute. Second, distances between the projected features locally approximate δ_{AIRM} and, therefore, inherit its invariance properties (e.g., affine mixing) [41]. This improves upon a LogEig layer [37] which projects features to the tangent space at the identity matrix. As a result, distances between LogEig projected features correspond to distances measured with the log-Euclidean Riemannian metric (LERM) [51] which is not invariant to affine mixing. Third, controlling the Fréchet variance in (17) empirically speeds up learning and improves generalization [48].

4 SPDDSMBN to crack interpretable MSMTUDA for EEG data

With SPDDSMBN introduced in the previous section, we focus on a specific application domain, namely, MSMTUDA for EEG-based BCIs and propose an intrinsically interpretable architecture which we denote TSMNet.

Generative model of EEG EEG signals $\mathbf{x}(t) \in \mathbb{R}^P$ capture voltage fluctuations on P channels. A EEG record (=domain) is uniquely identified by a subject and session identifier. After standard pre-processing steps, each domain i contains $j = 1, \dots, M$ labeled observations with features $\mathbf{X}_{ij} \in \mathcal{X} \subset \mathbb{R}^{P \times T}$ where T is the number of temporal samples. Due to linearity of Maxwell's equations and Ohmic conductivity of tissue layers in the frequency ranges relevant for EEG [52], a domain-specific linear instantaneous mixture of sources model is a valid generative model:

$$\mathbf{X}_{ij} = \mathbf{A}_i \mathbf{S}_{ij} + \mathbf{N}_{ij} \quad (18)$$

where $\mathbf{S}_{ij} \in \mathbb{R}^{Q \times T}$ represents the activity of Q latent sources, $\mathbf{A}_i \in \mathbb{R}^{P \times Q}$ a domain-specific mixing matrix and $\mathbf{N}_{ij} \in \mathbb{R}^{P \times T}$ additive noise. Both \mathbf{A}_i and \mathbf{S}_{ij} are unknown which demands making assumptions on \mathbf{A}_i (e.g., anatomical prior knowledge [53]) and/or \mathbf{S}_{ij} (e.g., statistical independence [54]) to extract interesting sources.

⁴To preserve the norm, the off diagonal elements are scaled by $\sqrt{2}$.

Interpretable MSMTUDA for EEG data As label information is available for the source domains, our goal is to identify discriminative oscillatory sources shared across domains. Our approach relies on TSM models with linear classifiers [12], as they are consistent [13] and intrinsically interpretable [17] estimators for generative models with log-linear relationships between the target y and variance $\text{Var}\{s^{(k)}(t)\}$ of $k = 1, \dots, K \leq Q$ discriminative sources. We, therefore, constrain our hypothesis class \mathcal{H} to functions $h : \mathcal{X} \times \mathcal{I}_d \rightarrow \mathcal{Y}$ that can be decomposed into a composition of a shared linear feature extractor with covariance pooling $f_\theta : \mathcal{X} \rightarrow \mathcal{S}_D^+$, domain-specific tangent space mapping $m_\phi : \mathcal{S}_D^+ \times \mathcal{I}_d \rightarrow \mathbb{R}^{D(D+1)/2}$, and a shared linear classifier $g_\psi : \mathbb{R}^{D(D+1)/2} \rightarrow \mathcal{Y}$ with parameters $\Theta = \{\theta, \phi, \psi\}$.

TSMNet with SPDDSMBN Unlike previous approaches which learn f_θ, m_ϕ, g_ψ sequentially [29, 31, 13, 30], we parametrize $h = g_\psi \circ m_\phi \circ f_\theta$ as a neural network and learn the entire model in an end-to-end fashion (Figure 1b). Details of the proposed architecture, denoted TSMNet, are provided in appendix A.2.4. In a nutshell, we parametrize f_θ as the composition of the first two linear convolutional layers of ShConvNet [55], covariance pooling [56], BiMap [37], and ReEig [37] layers. A BiMap layer applies a linear subspace projection, and a ReEig layer thresholds eigenvalues of symmetric matrices so that the output is SPD. We used the default threshold (10^{-4}) and found that it was never active in the trained models. Hence, after training, f_θ fulfilled the hypothesis class constraints. In order for m_ϕ to align the domain data and compute TSM, we use SPDDSMBN (13) with shared parameters (i.e., $\mathbf{G}_{\phi_i} = \mathbf{G}_\phi = \mathbf{I}, \nu_{\phi_i} = \nu_\phi$) in (17). Finally, the classifier g_ψ was parametrized as a linear layer with softmax activations. We use the standard-cross entropy loss as training objective, and optimized the parameters with the Riemannian ADAM optimizer [57].

5 Experiments with EEG data

In the following, we apply our method to classify target labels from short segments of EEG data. We consider two BCI applications, namely, mental imagery [5] and mental workload estimation [58]. Both applications have high potential to aid society but have, currently, limited practical value because of poor generalization across sessions and subjects [19, 15].

Datasets and preprocessing The considered mental imagery datasets were BNCI2014001 [59] (9 subjects/2 sessions/4 classes), BNCI2015001 [60] (12/2-3/2), Lee2019 [61] (54/2/2), Lehner2020 [62] (1/7/2), Stieger2021 [63] (62/4-8/4) and Hehnberger2021 [64] (1/26/4). For mental workload estimation, we used a recent competition dataset [65] (12/2/3). A detailed description of the datasets is provided in appendix A.2.1. Altogether, we analyzed a total of 603 sessions of 158 human subjects whose data was acquired in previous studies that obtained the subjects' informed consent and the right to share anonymized data.

Python packages (moabb [14], mne [66]) were used to preprocess the datasets. The applied steps comprise resampling the EEG signals to 250/256 Hz, applying temporal filters to extract oscillatory EEG activity in the 4 to 36 Hz range (spectrally resolved if required by a method) and finally extract short segments ($\leq 3s$) associated to a class label (details provided in appendix A.2.2).

Evaluation We evaluated TSMNet against several baseline methods implementing direct transfer or multi-source (-target) UDA strategies. They can be broadly categorized as component based [67, 64], Riemannian geometry aware [12, 17, 30, 68] or deep learning [55, 69, 25]. All models were fit and evaluated with a randomized leave 5% of the sessions (inter-session TL) or subjects (inter-subject TL) out cross-validation (CV) scheme. For inter-session TL, the models were only provided with data of the associated subject. When required, inner train/test splits (neural nets) or CV (shallow methods) were used to optimize hyper parameters (e.g., early stopping, regularization parameters). The dataset Hehnberger2021 was used to fit the hyper parameters of TSMNet, and is, therefore, omitted in the presented results. Balanced accuracy (i.e., the average recall across classes) was used as scoring metric.

Soft- and hardware We either used publicly available python code or implemented the methods in python using the packages torch [70], scikit-learn [71], skorch [72], geoopt [73], mne [66], pyriemann [74], pymanopt [75]. We ran the experiments on standard computation PCs equipped with 32 core CPUs with 128 GB of RAM and used up to 1 GPU (24 GRAM). Depending on the dataset size, fitting and evaluating TSMNet varied from a few seconds to minutes.

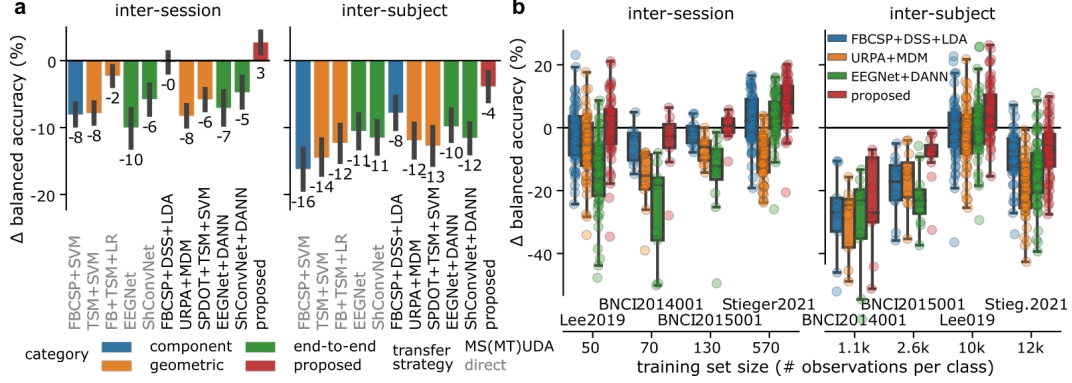


Figure 2: Mental imagery results (5 datasets). BCI test set score (balanced accuracy) for inter-session/-subject transfer learning methods relative to a SOA domain-specific reference model (=FB+TSM+LR; 80%/20% chronological train/test split). **a**, Barplots summarize the grand average (573 sessions, 138 subjects) results. Errorbars indicate bootstrapped ($1e3$ repetitions) 95% confidence intervals (over subjects). **b**, Box and scatter plots summarize the dataset-specific results for selected methods from each category. Datasets are ordered according to the training set size. Each dot summarizes the score for one subject. Lehner2021 is not displayed as it contains only 1 subject.

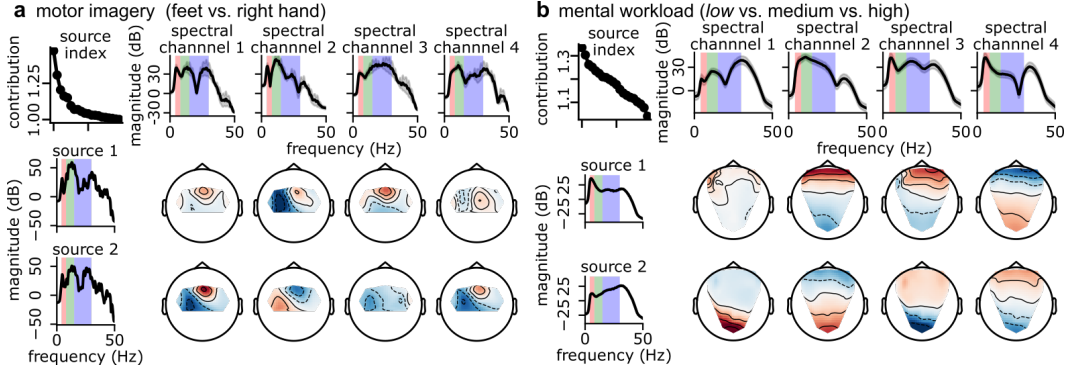


Figure 3: Model interpretation results. Patterns extracted from a fitted TSMNet(SPDDSMNB). **a**, Motor imagery dataset (BNCI2015001, inter-subject TL). The top, left panel lists the contribution of each extracted source ($n=20$) to the target class. Panels in the left column summarize the spectral patterns of extracted sources. For visualization purposes, only the 2 most discriminative sources are displayed. Panels in the top row summarize the frequency profile of each spectral channel (output of 4 temporal convolution layers in f_θ). Topographic plots summarize the spatial mixing coefficients for each source (=rows) and spectral channel (=columns). **b**, As in **a** but for the mental workload estimation dataset and class *low*.

5.1 Mental imagery

TSMNet closes the gap to domain-specific methods Figure 2 summarizes the mental imagery results. It displays test set scores of the considered TL methods relative to the score of a SOA domain-specific reference method. Combining the results of all subjects across datasets (Figure 2a), it becomes apparent that TSMNet is the only method that can significantly reduce the gap to the reference method (inter-session) or even exceed its performance (inter-subject). Figure 2b displays the results resolved across datasets (for details see appendix A.3.1). We make two important observations. First, concerning inter-session TL, TSMNet meets or exceeds the score of the reference method consistently across datasets. Second, concerning inter-subject TL, we found that all considered methods tend to reduce the performance gap as the dataset size (# subjects) increases, and that TSMNet is consistently the top or among the top methods. As a fitted TSMNet corresponds to a typical TSM model with a linear classifier, we can transform the fitted parameters into interpretable patterns [17]. Figure 3a displays extracted patterns for the BNCI2015001 dataset (inter-subject TL). It is clearly visible that TSMNet infers the target label from neurophysiologically plausible sources (rows in Figure 3a). As expected [2], the source with highest contribution has spectral peaks in the alpha and beta bands, and originates in contralateral and central sensorimotor cortex.

Table 1: Ablation study. Grand average (5 mental imagery datasets, 138 subjects, inter-session TL) score for the test data relative to the proposed method, and training fit time (50 epochs). Standard-deviation is used to report the variability across subjects. Permutation t-tests (1e4 perms, df=137, 4 tests with t-max adjustment) were used to identify significant effects.

\mathcal{S}_D^+	DSBN	BN method	Δ balanced accuracy (%)		fit time (s)
			mean (std)	t-val (p-val)	mean (std)
yes	yes	SPDMBN (algo. 1) (<i>proposed</i>)	-	-	16.9 (1.0)
	yes	SPDBN [48]	-1.6 (2.2)	-7.8 (0.0001)	20.3 (1.6)
	no	SPDMBN (algo. 1)	-3.9 (4.4)	-10.7 (0.0001)	11.3 (0.5)
no	yes	MBN [32]	-4.5 (3.8)	-10.1 (0.0001)	6.6 (0.2)
	no	MBN [32]	-6.9 (4.8)	-13.4 (0.0001)	4.4 (0.1)

DSBN on \mathcal{S}_D^+ drives the success of TSMNet Since TSMNet combines several advances, we present the results of an ablation study in Table 1. It summarizes the grand average inter-session TL test scores relative to TSMNet with SPDDSMNB for $n = 138$ subjects. We observed three significant effects. The largest effect can be attributed to \mathcal{S}_D^+ , as we observed the largest performance decline if the architecture would be modified⁵ to omit the SPD manifold (4.5% with DSBN, 3% w/o DSBN). The performance gain comes at the cost of a 2.6x longer time to fit the parameters. The second largest effect can be attributed to DSBN; without DSBN the performance dropped by 3.9% (with \mathcal{S}_D^+) and 2.4% (w/o \mathcal{S}_D^+). The smallest, yet significant effect can be attributed to SPDMBN.

5.2 Mental workload estimation

Compared to the baseline methods, TSMNet obtained the highest average scores of 54.7% (7.3%) and 52.4% (8.8%) in inter-session and -subject TL (for details see appendix A.3.1). Interestingly, the inter-session TL score of TSMNet matches the score (54.3%) of the winning method in last year’s competition [15]. To shed light on the sources utilized by TSMNet, we show patterns for a fitted model in Figure 3b. For the low mental workload class, the top contributing source’s activity peaked in the theta band and originated in pre-frontal areas. The second source’s activity originated in occipital cortex with non-focal spectral profile. Our results agree with the findings of previous research, as both areas and the theta band have been implicated in mind wandering and effort withdrawal [58].

6 Discussion

In this contribution, we proposed a machine learning framework around (domain-specific) momentum batch normalization on \mathcal{S}_D^+ to learn tangent space mapping (TSM) models and feature extractors in an end-to-end fashion. In a theoretical analysis, we provided error bounds as well as convergence guarantees under reasonable assumptions. We then applied the framework, to a multi-source multi-target unsupervised domain adaptation problem, namely, inter-session and -subject transfer learning for EEG data and obtained or attained state-of-the-art performance with a simple, intrinsically interpretable model, denoted TSMNet, in a total of 6 diverse BCI datasets (138 human subjects, 573 sessions). In the case of mental imagery, we found that TSMNet significantly reduced (inter-subject TL) or even exceeded (inter-session TL) the performance gap to a SOA domain-specific method. Although our framework could be readily extended to online UDA for unseen target domains, we limited this study to offline evaluations and leave actual BCI studies to future work. A limitation of our framework, and also any other method that involves eigen decomposition, is the computational complexity, which limits its application to high-dimensional SPD features (e.g., fMRI connectivity matrices with fine spatial granularity). Altogether, the presented results demonstrate the utility of our framework and in particular TSMNet as it not only achieves highly competitive results but is also intrinsically interpretable. While we do not foresee any immediate negative societal impacts, we provide direct contributions towards the scalability and acceptability of EEG-based healthcare and consumer technologies.

⁵To do so, we replaced the covariance pooling, BiMap, ReEig, SPD(DS)MBN, LogEig layers with variance pooling, elementwise log activations followed by (DS)MBN. Note that the resulting architecture is similar to ShConvNet.

Acknowledgments and Disclosure of Funding

References

- [1] Donald L. Schomer and Fernando H. Lopes da Silva. *Niedermeyer's Electroencephalography: basic principles, clinical applications, and related fields*. Lippincott Williams & Wilkins, 7 edition, 2018. ISBN 978-0-19-022848-4. doi: 10.1212/WNL.0b013e31822f0490.
- [2] G Pfurtscheller and F H Lopes. Event-related EEG / MEG synchronization and. *Clinical Neurophysiology*, 110:10576479, 1999.
- [3] Josef Faller, Jennifer Cummings, Sameer Saproo, and Paul Sajda. Regulation of arousal via online neurofeedback improves human performance in a demanding sensory-motor task. *Proceedings of the National Academy of Sciences*, 116(13):6482–6490, 2019. doi: 10.1073/pnas.1817207116.
- [4] Yu Zhang, Wei Wu, Russell T. Toll, Sharon Naparstek, Adi Maron-Katz, Mallissa Watts, Joseph Gordon, Jisoo Jeong, Laura Astolfi, Emmanuel Shpigel, Parker Longwell, Kamron Sarhadi, Dawlat El-Said, Yuanqing Li, Crystal Cooper, Cherise Chin-Fatt, Martijn Arns, Madeleine S. Goodkind, Madhukar H. Trivedi, Charles R. Marmar, and Amit Etkin. Identification of psychiatric disorder subtypes from functional connectivity patterns in resting-state electroencephalography. *Nature Biomedical Engineering*, 5(4):309–323, 2021. doi: 10.1038/s41551-020-00614-8.
- [5] Jonathan R Wolpaw, Niels Birbaumer, Dennis J McFarland, Gert Pfurtscheller, and Theresa M Vaughan. Brain-computer interfaces for communication and control. *Clinical neurophysiology : official journal of the International Federation of Clinical Neurophysiology*, 113:767–791, 2002. doi: doi:10.1016/s1388-2457(02)00057-3.
- [6] Shai Ben-David, John Blitzer, Koby Crammer, Alex Kulesza, Fernando Pereira, and Jennifer Wortman Vaughan. A theory of learning from different domains. *Machine Learning*, 79(1-2):151–175, 2010. doi: 10.1007/s10994-009-5152-4.
- [7] Judy Hoffman, Mehryar Mohri, and Ningshan Zhang. Algorithms and theory for multiple-source adaptation. In S. Bengio, H. Wallach, H. Larochelle, K. Grauman, N. Cesa-Bianchi, and R. Garnett, editors, *Advances in Neural Information Processing Systems*, volume 31. Curran Associates, Inc., 2018.
- [8] Dongrui Wu, Yifan Xu, and Bao-Liang Lu. Transfer Learning for EEG-Based Brain-Computer Interfaces: A Review of Progress Made Since 2016. *IEEE Transactions on Cognitive and Developmental Systems*, pages 1–1, 2020. doi: 10.1109/TCDS.2020.3007453.
- [9] Christa Neuper, Reinhold Scherer, Miriam Reiner, and Gert Pfurtscheller. Imagery of motor actions: Differential effects of kinesthetic and visual–motor mode of imagery in single-trial EEG. *Cognitive Brain Research*, 25(3):668–677, 2005. doi: 10.1016/j.cogbrainres.2005.08.014.
- [10] F Lotte, L Bougrain, A Cichocki, M Clerc, M Congedo, A Rakotomamonjy, and F Yger. A review of classification algorithms for EEG-based brain–computer interfaces: a 10 year update. *Journal of Neural Engineering*, 15(3):031005, 2018. doi: 10.1088/1741-2552/aab2f2.
- [11] Karina Statthaler, Andreas Schwarz, David Steyrl, Reinmar J. Kobler, Maria Katharina Höller, Julia Brandstetter, Lea Hehenberger, Marvin Bigga, and Gernot Müller-Putz. Cybathlon experiences of the Graz BCI racing team Mirage91 in the brain-computer interface discipline. *Journal of NeuroEngineering and Rehabilitation*, 14(1):129, 2017. doi: 10.1186/s12984-017-0344-9.
- [12] Alexandre Barachant, Stéphane Bonnet, Marco Congedo, and Christian Jutten. Multiclass brain-computer interface classification by Riemannian geometry. *IEEE transactions on bio-medical engineering*, 59(4):920–928, 2012. doi: 10.1109/TBME.2011.2172210.
- [13] David Sabbagh, Pierre Ablin, Gaël Varoquaux, Alexandre Gramfort, and Denis A Engemann. Manifold-regression to predict from MEG/EEG brain signals without source modeling. In *Advances in Neural Information Processing Systems*, pages 7323–7334, 2019.
- [14] Vinay Jayaram and Alexandre Barachant. MOABB: trustworthy algorithm benchmarking for BCIs. *Journal of Neural Engineering*, 15(6):066011, 2018. doi: 10.1088/1741-2552/aadea0.

- [15] Raphaëlle N. Roy, Marcel F. Hinss, Ludovic Darnet, Simon Ladouce, Emilie S. Jahanpour, Bertille Somon, Xiaoqi Xu, Nicolas Drougard, Frédéric Dehais, and Fabien Lotte. Retrospective on the First Passive Brain-Computer Interface Competition on Cross-Session Workload Estimation. *Frontiers in Neuroergonomics*, 3:838342, 2022. doi: 10.3389/fnrgo.2022.838342.
- [16] Marco Congedo, Alexandre Barachant, and Rajendra Bhatia. Riemannian geometry for EEG-based brain-computer interfaces; a primer and a review. *Brain-Computer Interfaces*, 4(3): 155–174, 2017. doi: 10.1080/2326263X.2017.1297192.
- [17] Reinmar J. Kobler, Jun-Ichiro Hirayama, Lea Hehenberger, Catarina Lopes-Dias, Gernot Müller-Putz, and Motoaki Kawanabe. On the interpretation of linear Riemannian tangent space model parameters in M/EEG. In *Proceedings of the 43rd Annual International Conference of the IEEE Engineering in Medicine and Biology Society (EMBC)*. IEEE, 2021. doi: 10.1109/EMBC46164.2021.9630144.
- [18] Stephen H. Fairclough and Fabien Lotte. Grand Challenges in Neurotechnology and System Neuroergonomics. *Frontiers in Neuroergonomics*, 1:602504, 2020. doi: 10.3389/fnrgo.2020.602504.
- [19] Xiaoxi Wei, A. Aldo Faisal, Moritz Grosse-Wentrup, Alexandre Gramfort, Sylvain Chevallier, Vinay Jayaram, Camille Jeunet, Stylianos Bakas, Siegfried Ludwig, Konstantinos Barmpas, Mehdi Bahri, Yannis Panagakis, Nikolaos Laskaris, Dimitrios A. Adamos, Stefanos Zafeiriou, William C. Duong, Stephen M. Gordon, Vernon J. Lawhern, Maciej Śliwowski, Vincent Rouanne, and Piotr Tempczyk. 2021 BEETL Competition: Advancing Transfer Learning for Subject Independence & Heterogenous EEG Data Sets. *arXiv:2202.12950 [cs, eess]*, 2022.
- [20] Vinay Jayaram, Morteza Alamgir, Yasemin Altun, Bernhard Scholkopf, and Moritz Grosse-Wentrup. Transfer Learning in Brain-Computer Interfaces Abstract\uFFFFDThe performance of brain-computer interfaces (BCIs) improves with the amount of avail. *IEEE Computational Intelligence Magazine*, 11(1):20–31, 2016. doi: 10.1109/MCI.2015.2501545.
- [21] Siamac Fazli, Florin Popescu, Márton Danóczy, Benjamin Blankertz, Klaus-Robert Müller, and Cristian Grozea. Subject-independent mental state classification in single trials. *Neural Networks*, 22(9):1305–1312, 2009. doi: 10.1016/j.neunet.2009.06.003.
- [22] Wojciech Samek, Motoaki Kawanabe, and Klaus Robert Müller. Divergence-based framework for common spatial patterns algorithms. *IEEE Reviews in Biomedical Engineering*, 7:50–72, 2014. doi: 10.1109/RBME.2013.2290621.
- [23] O-Yeon Kwon, Min-Ho Lee, Cuntai Guan, and Seong-Whan Lee. Subject-Independent Brain-Computer Interfaces Based on Deep Convolutional Neural Networks. *IEEE Transactions on Neural Networks and Learning Systems*, 31(10):3839–3852, 2020. doi: 10.1109/TNNLS.2019.2946869.
- [24] Sicheng Zhao, Bo Li, Colorado Reed, Pengfei Xu, and Kurt Keutzer. Multi-source Domain Adaptation in the Deep Learning Era: A Systematic Survey, 2020.
- [25] Ozan Ozdenizci, Ye Wang, Toshiaki Koike-Akino, and Deniz Erdogmus. Learning Invariant Representations From EEG via Adversarial Inference. *IEEE Access*, 8:27074–27085, 2020. doi: 10.1109/ACCESS.2020.2971600.
- [26] Lichao Xu, Zhen Ma, Jiayuan Meng, Minpeng Xu, Tzyy-Ping Jung, and Dong Ming. Improving Transfer Performance of Deep Learning with Adaptive Batch Normalization for Brain-computer Interfaces *. In *2021 43rd Annual International Conference of the IEEE Engineering in Medicine & Biology Society (EMBC)*, pages 5800–5803, Mexico, 2021. IEEE. ISBN 978-1-72811-179-7. doi: 10.1109/EMBC46164.2021.9629529.
- [27] Lichao Xu, Minpeng Xu, Yufeng Ke, Xingwei An, Shuang Liu, and Dong Ming. Cross-Dataset Variability Problem in EEG Decoding With Deep Learning. *Frontiers in Human Neuroscience*, 14:103, 2020. doi: 10.3389/fnhum.2020.00103.
- [28] Ravikiran Mane, Effie Chew, Karen Chua, Kai Keng Ang, Neethu Robinson, A. P. Vinod, Seong-Whan Lee, and Cuntai Guan. FBCNet: A Multi-view Convolutional Neural Network for Brain-Computer Interface. *arXiv:2104.01233 [cs, eess]*, 2021.

- [29] Paolo Zanini, Marco Congedo, Christian Jutten, Salem Said, and Yannick Berthoumieu. Transfer Learning: A Riemannian Geometry Framework With Applications to Brain–Computer Interfaces. *IEEE Transactions on Biomedical Engineering*, 65(5):1107–1116, 2018. doi: 10.1109/TBME.2017.2742541.
- [30] Pedro Luiz Coelho Rodrigues, Christian Jutten, and Marco Congedo. Riemannian Procrustes Analysis: Transfer Learning for Brain–Computer Interfaces. *IEEE Transactions on Biomedical Engineering*, 66(8):2390–2401, 2019. doi: 10.1109/TBME.2018.2889705.
- [31] Or Yair, Mirela Ben-Chen, and Ronen Talmon. Parallel Transport on the Cone Manifold of SPD Matrices for Domain Adaptation. *IEEE Transactions on Signal Processing*, 67(7):1797–1811, 2019. doi: 10.1109/TSP.2019.2894801.
- [32] Hongwei Yong, Jianqiang Huang, Deyu Meng, Xiansheng Hua, and Lei Zhang. Momentum Batch Normalization for Deep Learning with Small Batch Size. In Andrea Vedaldi, Horst Bischof, Thomas Brox, and Jan-Michael Frahm, editors, *Computer Vision – ECCV 2020*, volume 12357, pages 224–240. Springer International Publishing, Cham, 2020. ISBN 978-3-030-58609-6 978-3-030-58610-2. doi: 10.1007/978-3-030-58610-2_14.
- [33] He He and Dongrui Wu. Transfer Learning for Brain–Computer Interfaces: A Euclidean Space Data Alignment Approach. *IEEE Transactions on Biomedical Engineering*, 67(2):399–410, 2020. doi: 10.1109/TBME.2019.2913914.
- [34] Stylianos Bakas, Siegfried Ludwig, Konstantinos Barmpas, Mehdi Bahri, Yannis Panagakis, Nikolaos Laskaris, Dimitrios A. Adamos, and Stefanos Zafeiriou. Team Cogitat at NeurIPS 2021: Benchmarks for EEG Transfer Learning Competition, 2022.
- [35] Michael M. Bronstein, Joan Bruna, Yann LeCun, Arthur Szlam, and Pierre Vandergheynst. Geometric Deep Learning: Going beyond Euclidean data. *IEEE Signal Processing Magazine*, 34(4):18–42, 2017. doi: 10.1109/MSP.2017.2693418.
- [36] Ce Ju and Cuntai Guan. Tensor-CSPNet: A Novel Geometric Deep Learning Framework for Motor Imagery Classification. *arXiv:2202.02472 [cs, eess]*, 2022.
- [37] Zhiwu Huang and Luc Van Gool. A Riemannian Network for SPD Matrix Learning. In *Proceedings of the Thirty-First AAAI Conference on Artificial Intelligence*, AAAI’17, pages 2036–2042. AAAI Press, 2017.
- [38] Woong-Gi Chang, Tackgeun You, Seonguk Seo, Suha Kwak, and Bohyung Han. Domain-Specific Batch Normalization for Unsupervised Domain Adaptation. In *Proceedings of the IEEE/CVF Conference on Computer Vision and Pattern Recognition (CVPR)*, 2019.
- [39] Rajendra Bhatia. *Positive definite matrices*. Princeton university press, 2009.
- [40] P-A Absil, Robert Mahony, and Rodolphe Sepulchre. *Optimization algorithms on matrix manifolds*. Princeton University Press, 2009.
- [41] Xavier Pennec, Pierre Fillard, and Nicholas Ayache. A Riemannian framework for tensor computing. *International Journal of computer vision*, 66(1):41–66, 2006.
- [42] Hermann Karcher. Riemannian center of mass and mollifier smoothing. *Communications on pure and applied mathematics*, 30(5):509–541, 1977.
- [43] Sergey Ioffe and Christian Szegedy. Batch normalization: Accelerating deep network training by reducing internal covariate shift. In *International conference on machine learning*, pages 448–456. PMLR, 2015.
- [44] Shibani Santurkar, Dimitris Tsipras, Andrew Ilyas, and Aleksander Mądry. How Does Batch Normalization Help Optimization? In *Proceedings of the 32nd International Conference on Neural Information Processing Systems*, NIPS’18, pages 2488–2498, Red Hook, NY, USA, 2018. Curran Associates Inc.

- [45] Sergey Ioffe. Batch Renormalization: Towards Reducing Minibatch Dependence in Batch-Normalized Models. In *Proceedings of the 31st International Conference on Neural Information Processing Systems, NIPS'17*, pages 1942–1950, Red Hook, NY, USA, 2017. Curran Associates Inc. ISBN 978-1-5108-6096-4.
- [46] Daniel Brooks, Olivier Schwander, Frederic Barbaresco, Jean-Yves Schneider, and Matthieu Cord. Riemannian batch normalization for SPD neural networks. In *Advances in Neural Information Processing Systems*, volume 32. Curran Associates, Inc., 2019.
- [47] Shun-ichi Amari. *Information geometry and its applications*, volume 194. Springer, 2016.
- [48] Reinmar J. Kobler, Jun-ichiro Hirayama, and Motoaki Kawanabe. Controlling The Fréchet Variance Improves Batch Normalization on the Symmetric Positive Definite Manifold. In *ICASSP 2022 - 2022 IEEE International Conference on Acoustics, Speech and Signal Processing (ICASSP)*, pages 3863–3867, Singapore, Singapore, 2022. IEEE. ISBN 978-1-66540-540-9. doi: 10.1109/ICASSP43922.2022.9746629.
- [49] Catalin Ionescu, Orestis Vantzos, and Cristian Sminchisescu. Matrix Backpropagation for Deep Networks with Structured Layers. In *2015 IEEE International Conference on Computer Vision (ICCV)*, pages 2965–2973, Santiago, Chile, 2015. IEEE. ISBN 978-1-4673-8391-2. doi: 10.1109/ICCV.2015.339.
- [50] Jeffrey Ho, Guang Cheng, Hesamoddin Salehian, and Baba Vemuri. Recursive Karcher Expectation Estimators And Geometric Law of Large Numbers. In Carlos M. Carvalho and Pradeep Ravikumar, editors, *Proceedings of the Sixteenth International Conference on Artificial Intelligence and Statistics*, volume 31 of *Proceedings of Machine Learning Research*, pages 325–332, Scottsdale, Arizona, USA, 2013. PMLR.
- [51] Vincent Arsigny, Pierre Fillard, Xavier Pennec, and Nicholas Ayache. Geometric Means in a Novel Vector Space Structure on Symmetric Positive-Definite Matrices. *SIAM Journal on Matrix Analysis and Applications*, 29(1):328–347, 2007. doi: 10.1137/050637996.
- [52] Paul L. Nunez and Ramesh Srinivasan. *Electric Fields of the Brain*. Oxford University Press, 2006. ISBN 978-0-19-505038-7. doi: 10.1093/acprof:oso/9780195050387.001.0001.
- [53] Christoph M. Michel, Micah M. Murray, Göran Lantz, Sara Gonzalez, Laurent Spinelli, and Rolando Grave De Peralta. EEG source imaging. *Clinical Neurophysiology*, 115(10), 2004. doi: 10.1016/j.clinph.2004.06.001.
- [54] A. Hyvärinen and E. Oja. Independent component analysis: algorithms and applications. *Neural Networks*, 13(4-5):411–430, 2000. doi: 10.1016/S0893-6080(00)00026-5.
- [55] Robin Tibor Schirrmeister, Jost Tobias Springenberg, Lukas Dominique Josef Fiederer, Martin Glasstetter, Katharina Eggensperger, Michael Tangermann, Frank Hutter, Wolfram Burgard, and Tonio Ball. Deep learning with convolutional neural networks for EEG decoding and visualization: Convolutional Neural Networks in EEG Analysis. *Human Brain Mapping*, 38(11):5391–5420, 2017. doi: 10.1002/hbm.23730.
- [56] Dinesh Acharya, Zhiwu Huang, Danda Pani Paudel, and Luc Van Gool. Covariance Pooling for Facial Expression Recognition. In *Proceedings of the IEEE Conference on Computer Vision and Pattern Recognition (CVPR) Workshops*, 2018.
- [57] Gary Becigneul and Octavian-Eugen Ganea. Riemannian Adaptive Optimization Methods. In *International Conference on Learning Representations*, 2019.
- [58] Frédéric Dehais, Alex Lafont, Raphaëlle Roy, and Stephen Fairclough. A Neuroergonomics Approach to Mental Workload, Engagement and Human Performance. *Frontiers in Neuroscience*, 14:268, 2020. doi: 10.3389/fnins.2020.00268.
- [59] Michael Tangermann, Klaus-Robert Müller, Ad Aertsen, Niels Birbaumer, Christoph Braun, Clemens Brunner, Robert Leeb, Carsten Mehring, Kai J Miller, Gernot Müller-Putz, Guido Nolte, Gert Pfurtscheller, Hubert Preissl, Gerwin Schalk, Alois Schlögl, Carmen Vidaurre, Stephan Waldert, and Benjamin Blankertz. Review of the BCI Competition IV. *Frontiers in Neuroscience*, 6, 2012.

- [60] Josef Faller, Carmen Vidaurre, Teodoro Solis-Escalante, Christa Neuper, and Reinhold Scherer. Autocalibration and recurrent adaptation: towards a plug and play online ERD-BCI. *Neural Systems and Rehabilitation Engineering, IEEE Transactions on*, 20(3):313–319, 2012.
- [61] Min-Ho Lee, O-Yeon Kwon, Yong-Jeong Kim, Hong-Kyung Kim, Young-Eun Lee, John Williamson, Siamac Fazli, and Seong-Whan Lee. EEG dataset and OpenBMI toolbox for three BCI paradigms: an investigation into BCI illiteracy. *GigaScience*, 8(5):giz002, 2019. doi: 10.1093/gigascience/giz002.
- [62] Rea Lehner, Neethu Robinson, Tushar Chouhan, Mihelj Mihelj, Ernest, Kratka Kratka, Paulina, Frédéric Debraïne, Cuntai Guan, and Nicole Wenderoth. Design considerations for long term non-invasive Brain Computer Interface training with tetraplegic CYBATHLON pilot: CYBATHLON 2020 Brain-Computer Interface Race Calibration Paradigms. 2020. doi: 10.3929/ETHZ-B-000458693. URL <http://hdl.handle.net/20.500.11850/458693>. Medium: application/vnd.openxmlformats-officedocument.wordprocessingml.document,application/octet-stream,application/zip,text/plain,2.93 GB Publisher: ETH Zurich.
- [63] James R. Stieger, Stephen A. Engel, and Bin He. Continuous sensorimotor rhythm based brain computer interface learning in a large population. *Scientific Data*, 8(1):98, 2021. doi: 10.1038/s41597-021-00883-1.
- [64] Lea Hehenberger, Reinmar J. Kobler, Catarina Lopes-Dias, Nitikorn Srisrisawang, Peter Tumfart, John B. Uroko, Paul R. Torke, and Gernot R. Müller-Putz. Long-term mutual training for the CYBATHLON BCI Race with a tetraplegic pilot: a case study on inter-session transfer and intra-session adaptation. *Frontiers in Human Neuroscience*, 2021. doi: 10.3389/fnhum.2021.635777.
- [65] Marcel F. Hinss, Ludovic Darnet, Bertille Somon, Emilie Jahanpour, Fabien Lotte, Simon Ladouce, and Raphaëlle N. Roy. An EEG dataset for cross-session mental workload estimation: Passive BCI competition of the Neuroergonomics Conference 2021. 2021. doi: 10.5281/ZENODO.5055046.
- [66] Alexandre Gramfort. MEG and EEG data analysis with MNE-Python. *Frontiers in Neuroscience*, 7, 2013. doi: 10.3389/fnins.2013.00267.
- [67] Kai Keng Ang, Zhang Yang Chin, Haihong Zhang, and Cuntai Guan. Filter Bank Common Spatial Pattern (FBCSP) in Brain-Computer Interface. In *2008 IEEE International Joint Conference on Neural Networks (IEEE World Congress on Computational Intelligence)*, pages 2390–2397, Hong Kong, China, 2008. IEEE. ISBN 978-1-4244-1820-6. doi: 10.1109/IJCNN.2008.4634130.
- [68] Or Yair, Felix Dietrich, Ronen Talmon, and Ioannis G. Kevrekidis. Domain Adaptation with Optimal Transport on the Manifold of SPD matrices. *arXiv:1906.00616 [cs, stat]*, 2020.
- [69] Vernon J Lawhern, Amelia J Solon, Nicholas R Waytowich, Stephen M Gordon, Chou P Hung, and Brent J Lance. EEGNet: a compact convolutional neural network for EEG-based brain–computer interfaces. *Journal of Neural Engineering*, 15(5):056013, 2018. doi: 10.1088/1741-2552/aace8c.
- [70] Adam Paszke, Sam Gross, Francisco Massa, Adam Lerer, James Bradbury, Gregory Chanan, Trevor Killeen, Zeming Lin, Natalia Gimelshein, Luca Antiga, Alban Desmaison, Andreas Kopf, Edward Yang, Zachary DeVito, Martin Raison, Alykhan Tejani, Sasank Chilamkurthy, Benoit Steiner, Lu Fang, Junjie Bai, and Soumith Chintala. PyTorch: An Imperative Style, High-Performance Deep Learning Library. In H. Wallach, H. Larochelle, A. Beygelzimer, F. d’Alché-Buc, E. Fox, and R. Garnett, editors, *Advances in Neural Information Processing Systems* 32, pages 8024–8035. Curran Associates, Inc., 2019.
- [71] F. Pedregosa, G. Varoquaux, A. Gramfort, V. Michel, B. Thirion, O. Grisel, M. Blondel, P. Prettenhofer, R. Weiss, V. Dubourg, J. Vanderplas, A. Passos, D. Cournapeau, M. Brucher, M. Perrot, and E. Duchesnay. Scikit-learn: Machine Learning in Python. *Journal of Machine Learning Research*, 12:2825–2830, 2011.

- [72] Marian Tietz, Thomas J. Fan, Daniel Nouri, Benjamin Bossan, and skorch Developers. *skorch: A scikit-learn compatible neural network library that wraps PyTorch*. 2017. URL <https://skorch.readthedocs.io/en/stable/>.
- [73] Max Kochurov, Rasul Karimov, and Serge Kozlukov. Geoopt: Riemannian Optimization in PyTorch, 2020. _eprint: 2005.02819.
- [74] Barachant Alexandre. pyRiemann, 2022. URL <https://github.com/pyRiemann/pyRiemann>.
- [75] James Townsend, Niklas Koep, and Sebastian Weichwald. Pymanopt: A python toolbox for optimization on manifolds using automatic differentiation. *Journal of Machine Learning Research*, 17(137):1–5, 2016.
- [76] Yaroslav Ganin, Evgeniya Ustinova, Hana Ajakan, Pascal Germain, Hugo Larochelle, François Laviolette, Mario March, and Victor Lempitsky. Domain-Adversarial Training of Neural Networks. *Journal of Machine Learning Research*, 17(59):1–35, 2016.

A Supplementary Material

A.1 Proof of proposition 1

Let us quickly repeat the definitions, assumptions and proposition 1. We define a dataset containing the latent observations generated with feature set θ_k as $\mathcal{T}_{\theta_k} = \{f_{\theta_k}(\mathbf{x}) | \mathbf{x} \in \mathcal{T}\}$, and a minibatch of M iid samples drawn from \mathcal{T}_{θ_k} at training step k as \mathcal{B}_k . We denote the Fréchet mean of \mathcal{T}_{θ_k} as \mathbf{G}_{θ_k} , the Fréchet variance as $\text{Var}_{\theta_k}(\mathcal{T}_{\theta_k})$, and the estimated Fréchet mean, defined in (9), as \mathbf{G}_k , and the estimated batch mean as \mathbf{B}_k . We assume that the variance of the latent dataset $\mathcal{T}_{\theta_{k-1}}$ at the previous training step with respect to \mathbf{G}_{θ_k} at the current training step is bounded by the current Fréchet variance and the norm of the differences in the parameters

$$\text{Var}_{\theta}(\mathcal{T}_{\theta_{k-1}}) \leq (1 + \|\theta_k - \theta_{k-1}\|) \text{Var}_{\theta}(\mathcal{T}_{\theta_k}) \quad (19)$$

Proposition 1 states then that the variance $\text{Var}_{\theta}(\mathbf{G}_k)$ of the running mean is non-increasing over training steps k if

$$\|\theta_k - \theta_{k-1}\| \leq \frac{1 - \gamma^2}{(1 - \gamma)^2} - 1 \quad (20)$$

holds true.

In the proof, we will use Theorem 2 of [50] which relates the distance between interpolated points along the geodesic $\mathbf{R} \#_{\gamma} \mathbf{S}$, connecting points \mathbf{R} and \mathbf{S} , and point \mathbf{T} to the distances between \mathbf{R} , \mathbf{S} and \mathbf{T} . Formally, for all $\mathbf{R}, \mathbf{S}, \mathbf{T} \in \mathcal{S}_D^+$ we have

$$\delta_{AIRM}^2(\mathbf{R} \#_{\gamma} \mathbf{S}, \mathbf{T}) \leq (1 - \gamma) \delta_{AIRM}^2(\mathbf{R}, \mathbf{T}) + \gamma \delta_{AIRM}^2(\mathbf{S}, \mathbf{T}) - \gamma(1 - \gamma) \delta_{AIRM}^2(\mathbf{R}, \mathbf{S}) \quad (21)$$

As a last ingredient for the proof, we use Proposition 1 of [50], which states that for a random variable \mathbf{Z} , following distribution $P_{\mathbf{Z}}$ defined on \mathcal{S}_D^+ with Fréchet mean $\mathbf{G}_{\mathbf{Z}}$, we have for any point $\mathbf{A} \in \mathcal{S}_D^+$

$$\mathbb{E}_{\mathbf{Z}}\{\delta_{AIRM}^2(\mathbf{Z}, \mathbf{A})\} \geq \underbrace{\int \delta_{AIRM}^2(\mathbf{z}, \mathbf{G}_{\mathbf{Z}}) dP_{\mathbf{Z}}(\mathbf{z})}_{=:\text{Var}(\mathbf{Z})} + \delta_{AIRM}^2(\mathbf{A}, \mathbf{G}_{\mathbf{Z}}) \quad (22)$$

which means that the expected distance between \mathbf{A} and \mathbf{Z} is bounded from below by the variance of \mathbf{Z} and the distance between \mathbf{A} and its Fréchet mean $\mathbf{G}_{\mathbf{Z}}$.

Proof of Proposition 1. We prove Proposition 1 via induction. We assume that the variance of \mathbf{G}_{k-1} , that is the expected distance between the running mean \mathbf{G}_{k-1} and the Fréchet mean \mathbf{G}_{θ_k} , is bounded by the variance of the batch mean \mathbf{G}_{k-1} :

$$\text{Var}_{\theta_k}(\mathbf{G}_{k-1}) = \mathbb{E}_{\mathbf{G}_{k-1}}\{\delta_{AIRM}^2(\mathbf{G}_{k-1}, \mathbf{G}_{\theta_k})\} \leq \text{Var}_{\theta_k}(\mathbf{B}_{k-1}) \quad (23)$$

and show that this also holds for \mathbf{G}_k and \mathbf{B}_k . The assumption is trivially satisfied for $\mathbf{G}_0 = \mathbf{B}_0$. We start the induction step with (21) and apply it to the update rule for the running estimate \mathbf{G}_k . As a result, we have

$$\delta^2(\mathbf{G}_k, \mathbf{G}_{\theta_k}) \leq (1 - \gamma)\delta^2(\mathbf{G}_{k-1}, \mathbf{G}_{\theta_k}) + \gamma\delta^2(\mathbf{B}_k, \mathbf{G}_{\theta_k}) - \gamma(1 - \gamma)\delta^2(\mathbf{G}_{k-1}, \mathbf{B}_k) \quad (24)$$

where we used δ^2 instead of δ_{AIRM}^2 for brevity, and $\mathbf{G}_k = \mathbf{G}_{k-1} \#_{\gamma} \mathbf{B}_k$, as defined in algorithm 1. By considering \mathbf{G}_k , \mathbf{G}_{k-1} and \mathbf{B}_k as random variables and taking expectations, we get

$$\text{Var}_{\theta_k}(\mathbf{G}_k) \leq (1 - \gamma)\text{Var}_{\theta_k}(\mathbf{G}_{k-1}) + \gamma\text{Var}_{\theta_k}(\mathbf{B}_k) - \gamma(1 - \gamma)\mathbb{E}_{\mathbf{G}_{k-1}}\{\mathbb{E}_{\mathbf{B}_k}\{\delta^2(\mathbf{G}_{k-1}, \mathbf{B}_k)\}\} \quad (25)$$

Using (22) to simplify the last term, we obtain

$$\text{Var}_{\theta_k}(\mathbf{G}_k) \leq (1 - \gamma)\text{Var}_{\theta_k}(\mathbf{G}_{k-1}) + \gamma\text{Var}_{\theta_k}(\mathbf{B}_k) - \gamma(1 - \gamma)(\text{Var}_{\theta_k}(\mathbf{G}_{k-1}) + \text{Var}_{\theta_k}(\mathbf{B}_k)) \quad (26)$$

$$\leq (1 - \gamma)^2\text{Var}_{\theta_k}(\mathbf{G}_{k-1}) + \gamma^2\text{Var}_{\theta_k}(\mathbf{B}_k) \quad (27)$$

Applying assumptions (23) and (19), we get

$$\text{Var}_{\theta_k}(\mathbf{G}_k) \stackrel{(23)}{\leq} (1 - \gamma)^2\text{Var}_{\theta_k}(\mathbf{B}_{k-1}) + \gamma^2\text{Var}_{\theta_k}(\mathbf{B}_k) \quad (28)$$

$$\stackrel{(19)}{\leq} [(1 - \gamma)^2(1 + \|\theta_k - \theta_{k-1}\|) + \gamma^2] \text{Var}_{\theta_k}(\mathbf{B}_k) \quad (29)$$

The resulting inequality holds true, for

$$(1 - \gamma)^2(1 + \|\theta_k - \theta_{k-1}\|) + \gamma^2 \stackrel{!}{\leq} 1 \Leftrightarrow \|\theta_k - \theta_{k-1}\| \stackrel{!}{\leq} \frac{1 - \gamma^2}{(1 - \gamma)^2} - 1 \quad (30)$$

and, in turn, results in feasible bounds for the parameter updates for fixed $\gamma \in (0, 1)$. This concludes the proof. \square

A.2 Supplementary Methods

A.2.1 Datasets

A summary of the datasets' key attributes is listed in Table 2. The datasets contain a diverse sample of 154 human subjects, whose data was acquired in Europe (38 subjects; BNCI2014001, BNCI2015001, Lehner2021, Hehenberger2021, Hinss2021), Asia (54 subjects; Lee2019) and North America (62 subjects; Stieger2021).

A.2.2 Preprocessing

Depending on the dataset, either all or a subset of EEG channels was selected, and then resampled along the temporal dimension to a sampling rate of either 250 or 256 Hz. (see Table 2). Thereafter, an infinite impulse response (IIR) bandpass filter was used to extract EEG activity in the 4 to 36 Hz range (4th order Butterworth filter, 4 and 36 Hz cut-off frequencies, zero-phase). Some baseline methods required spectrally resolved input data. For these, we applied a bank of 8 filters with similar parameters except for the cut-off frequencies ([4, 8], [8, 12], ..., [32, 36] Hz). Finally, short epochs (=segments) were extracted (see Table 2) relative to the task cues (=labels). The labeled data were then extended with a domain index (= unique integer associated to one session of one subject).

⁶We used 20 channels that covered sensorimotor areas.

⁷We used 34 channels that covered sensorimotor areas.

⁸To reduce computation time, only data from the 4th to last session were considered (inter-session) or last session (inter-subject).

⁹We used 30 channels with a dense coverage in frontal areas.

¹⁰The dataset is shared on an individual basis by the authors of [64].

A.2.3 Baseline methods

We considered several established and SOA baseline methods which were previously applied to inter-session/-subject TL. They can be broadly categorized as component based, Riemannian geometry aware or deep learning which we denote component, geometric and end-to-end, respectively. For the component category, we considered the popular filter-bank common spatial patterns (FBCSP+SVM) [67] and a variant [64], designed for MSMTUDA, that applies domain-specific standardization (DSS) to features before classification, denoted FBCSP+DSS+LDA. The geometric category was represented by TSM+SVM [12], a spectrally resolved variant [17] denoted FB+TSM+LR. We additionally considered two MSUDA methods, denoted URPA+MDM and SPDOT+TSM+SVM here, that align SPD observations (=spatial covariance matrices) of different domains. The former uses Riemannian Procrustes Analysis (RPA) [30] to align domains, and the latter optimal transport (OT) on S_D^+ [68]. The end-to-end category was represented by EEGNet [69] and ShConvNet [55] two convolutional neural network architectures specifically designed for EEG data. We additionally considered variants [25] that use domain-adversarial neural networks (DANN) [76] to learn domain-invariant latent representations.

A.2.4 TSMNet

Architecture The architecture of TSMNet is outlined in Figure 4 and detailed in Table 3. The feature extractor f_θ comprises two convolutional layers, followed by covariance pooling [56], BiMap [37] and ReEig [37] layers. The first convolutional layer performs convolution along the temporal dimension; implementing a finite impulse response (FIR) filter bank (4 filters) with learnable parameters. The second convolutional layer applies spatio-spectral filters (40 filters) along the spatial and convolutional channel dimensions. Covariance pooling is then applied along the temporal dimension. A subsequent BiMap layer projects covariance matrices to a subspace via a bilinear mapping (i.e., $\text{BiMap}(\mathbf{Z}) = \mathbf{W}_\theta^T \mathbf{Z} \mathbf{W}_\theta$) where the parameter matrix \mathbf{W}_θ is constrained to have orthogonal rows (i.e., $\mathbf{W}_\theta \in \{\mathbf{U} \in \mathbb{R}^{I \times O} : \mathbf{U}^T \mathbf{U} = \mathbf{I}_O, I \geq O\}$). Next, a ReEig layer rectifies all eigenvalues, lower than a threshold $\epsilon = 10^{-4}$ (i.e., $\text{ReEig}(\mathbf{Z}) = \mathbf{U}_{\max}(\Sigma, \epsilon \mathbf{I}) \mathbf{U}^T$ with $[\Sigma, \mathbf{U}] = \text{eig}(\mathbf{Z})$). Domain-specific tangent space mapping m_ϕ is implemented via combining SPDDSMBN and LogEig layers. In order for m_ϕ to align the domain data and compute TSM, we use SPDDSMBN (13) with shared parameters (i.e., $\mathbf{G}_{\phi_i} = \mathbf{G}_\phi = \mathbf{I}, \nu_{\phi_i} = \nu_\phi$) in (17). The classifier g_ψ was parametrized as a linear layer with softmax activations.

Parameter estimation We used the cross entropy loss as training objective, and the standard backpropagation framework with extensions for structured matrices [49] and manifold-constrained gradients [40] to propagate gradients through the layers of TSMNet. Gradients were estimated with mini-batches of fixed size (50 observations; 10 per domain; 5 distinct domains) and converted into parameter updates with the Riemannian ADAM optimizer [57] (10^{-3} learning rate, 10^{-4} weight decay applied to unconstrained parameters; $\beta_1 = 0.9, \beta_2 = 0.999$).

For every MSMTUDA problem, comprising source and target domain sets, we split the source domains' data into training and validation sets (80%/20% splits; randomized; stratified across domains and labels) and repeatedly iterated through the training set for 50 epochs via exhaustive minibatch sampling. As required by SPDMBN, we implemented a decaying schedule (over epochs) for the training momentum parameter $\gamma_{train}(k)$, defined in (12), with $\gamma_{train}(0) = 1$ and $\gamma_{min} = 0.2$ attained at epoch $K = 40$. During training, we monitored the loss on the validation data (at the end of every epoch). Post training, the model with minimal loss on the validation data was selected. For each target domain, the associated data was then passed through this model to estimate the labels. During the forward pass, the domain's normalization statistics within the SPDMBN layers were computed by solving (4) with the Karcher flow algorithm [42].

A.3 Supplementary results

A.3.1 EEG data

The test set score for each considered EEG dataset is summarized in in Table 4. Significant differences between the proposed method (TSMNet with SPDDSMBN) and baseline methods are highlighted.

¹¹Shared Frechet variance parameter ν_ϕ^2 .

Table 2: Dataset attributes. The epoch indices the temporal window after a task cue (time relative to cue onset) that was extracted from continuous EEG data.

dataset	epoch (s)	sampling rate (Hz)	channels #	subjects #	sessions #	observations # (per session)
BNCI2014001	0.5 - 3.5	250	22	9	2	288
BNCI2015001	1.0 - 4.0	256	13	12	2-3	200
Lee2019	1.0 - 3.5	250	20 ⁶	54	2	100
Stieger2021	1.0 - 3.0	250	34 ⁷	62	4-8 ⁸	390
Lehner2021	0.5 - 2.5	250	60	1	7	61
Hehenberger2021	1.0 - 3.0	250	32	1	26	105
Hinss2021	0.0 - 2.0	250	30 ⁹	15	2	447

dataset #	classes	license	identifier	linked publication
BNCI2014001	4	CC BY-ND 4.0	001-2014	[59]
BNCI2015001	2	CC BY-NC-ND 4.0	001-2015	[60]
Lee2019	2	unspecified	100542	[61]
Stieger2021	4	CC BY 4.0	m9.figshare.13123148.v1	[63]
Lehner2021	2	InC-NC	10.3929/ethz-b-000458693	[62]
Hehenberger2021	4	individual ¹⁰	-	[64]
Hinss2021	3	CC BY-SA 4.0	10.5281/zenodo.5055046	[65]

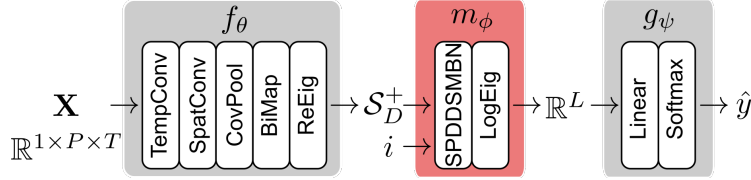


Figure 4: Overview of the TSMNet architecture. The network uses observations \mathbf{X} and the associated domain index i to estimate the target label \hat{y} .

Table 3: TSMNet architecture details. The letters P, T and C refer to the number of input channels, temporal samples and classes.

Block	Input (dim)	Output (dim)	Parameter (dim)	Operation	Note
TempConv	1 x P x T	4 x P x T	4 x 1 x 1 x 25	convolution	padding: same, reflect
SpatConv	4 x P x T	40 x 1 x T	40 x 4 x P x 1	convolution	padding: valid
CovPool	40 x T	40 x 40		covariance	temporal dimension
BiMap	40 x 40	20 x 20	40 x 20	bilinear	subspace projection
ReEig	20 x 20	20 x 20		EV threshold	threshold = 0.0001
SPDDSMBN	20 x 20	20 x 20	1 ¹¹	TSM	domain alignment
LogEig	20 x 20	210		TSM	
Linear	210	C	211 x C	linear	softmax activation

Table 4: Average (standard deviation across sessions or subjects) test set score (balanced accuracy; higher is better) for all BCI datasets and evaluations. Permutation-paired t-test were used to identify significant differences between the proposed (*highlighted*) and baseline methods (1e4 permutations, 10 tests, tmax correction). Significant differences are highlighted ($\bullet p \leq 0.05$, $\circ p \leq 0.01$, $\bullet p \leq 0.001$).

UDA	dataset evaluation degrees of freedom / # classes method	BNCI2014001		BNCI2015001	
		inter-session	inter-subject	inter-session	inter-subject
		17 / 4	8 / 4	27 / 2	11 / 2
no	FBCSP+SVM	\bullet 60.6 (4.9)	\bullet 32.3 (7.3)	\bullet 81.5 (4.4)	\bullet 58.6 (13.4)
	TSM+SVM	\bullet 61.8 (4.1)	\bullet 34.7 (8.6)	\bullet 75.7 (5.1)	\bullet 56.0 (6.0)
	FB+TSM+LR	69.8 (4.8)	\bullet 36.5 (8.2)	\bullet 80.9 (6.0)	\bullet 60.6 (10.9)
	EEGNet	\bullet 41.8 (5.8)	\bullet 43.3 (17.0)	\bullet 72.4 (8.4)	\bullet 59.2 (9.5)
	ShConvNet	\bullet 51.3 (2.3)	\bullet 42.2 (16.2)	\bullet 74.1 (4.2)	\bullet 58.7 (5.8)
yes	FBCSP+DSS+LDA	71.3 (1.8)	48.3 (14.3)	84.6 (4.8)	\bullet 67.7 (14.3)
	URPA+MDM	\bullet 59.5 (2.7)	46.8 (14.6)	\bullet 79.2 (4.6)	\bullet 70.3 (16.1)
	SPDOT+TSM+SVM	66.8 (3.8)	\bullet 38.6 (8.6)	\bullet 77.5 (2.9)	\bullet 63.3 (8.1)
	EEGNet+DANN	\bullet 50.0 (7.7)	45.8 (18.0)	\bullet 71.6 (5.3)	\bullet 63.7 (11.1)
	ShConvNet+DANN	\bullet 51.6 (3.2)	\bullet 42.2 (13.6)	\bullet 74.1 (4.0)	\bullet 64.2 (11.6)
	<i>TSMNet(SPDDSMBN)</i>	69.0 (3.6)	51.6 (16.5)	85.8 (4.3)	77.0 (13.7)
UDA	dataset evaluation degrees of freedom / # classes method	Lee2019		Stieger2021	
		inter-session	inter-subject	inter-session	inter-subject
		107 / 2	53 / 2	411 / 4	61 / 4
no	FBCSP+SVM	\bullet 63.1 (4.2)	\bullet 63.4 (12.1)	\bullet 47.5 (7.0)	\bullet 37.6 (10.5)
	TSM+SVM	\bullet 62.5 (3.3)	\bullet 65.3 (13.0)	\bullet 49.5 (8.1)	\bullet 40.2 (12.3)
	FB+TSM+LR	\bullet 65.2 (4.5)	\bullet 68.5 (12.4)	\bullet 57.3 (7.3)	\bullet 40.3 (9.2)
	EEGNet	\bullet 51.2 (2.7)	\bullet 69.6 (13.8)	\bullet 58.3 (7.9)	\bullet 43.1 (11.0)
	ShConvNet	\bullet 57.8 (4.0)	\bullet 68.5 (13.6)	\bullet 60.1 (6.6)	\bullet 42.2 (10.4)
yes	FBCSP+DSS+LDA	66.8 (4.1)	\bullet 68.7 (13.8)	\bullet 59.4 (6.6)	\bullet 48.2 (13.4)
	URPA+MDM	\bullet 63.8 (4.2)	\bullet 66.7 (12.3)	\bullet 47.0 (6.6)	\bullet 38.7 (10.4)
	SPDOT+TSM+SVM	\bullet 65.6 (4.2)	\bullet 65.4 (10.5)	\bullet 50.3 (5.8)	\bullet 42.1 (10.5)
	EEGNet+DANN	\bullet 55.4 (4.4)	\bullet 69.4 (13.1)	\bullet 60.1 (6.9)	\bullet 43.6 (10.7)
	ShConvNet+DANN	\bullet 59.1 (3.4)	\bullet 66.0 (12.4)	\bullet 61.3 (6.0)	\bullet 43.1 (11.5)
	<i>TSMNet(SPDDSMBN)</i>	68.2 (4.1)	74.6 (14.2)	64.8 (6.8)	48.9 (14.3)
UDA	dataset evaluation degrees of freedom / # classes method	Lehner2021	Hehen.2021	Hinss2021	
		inter-session	inter-session	inter-session	inter-subject
		6 / 2	25 / 4	29 / 3	14 / 3
no	FBCSP+SVM	68.9 (6.0)	\bullet 52.5 (7.1)	\bullet 43.7 (8.2)	45.6 (6.5)
	TSM+SVM	62.7 (9.1)	\bullet 44.8 (7.3)	\bullet 36.8 (4.5)	\bullet 41.7 (7.4)
	FB+TSM+LR	73.0 (9.6)	\bullet 52.2 (6.0)	\bullet 40.8 (7.1)	\bullet 45.1 (5.0)
	EEGNet	\bullet 49.6 (6.4)	\bullet 48.2 (6.3)	\bullet 46.3 (10.1)	47.8 (5.1)
	ShConvNet	\bullet 56.3 (7.3)	\bullet 53.0 (5.1)	48.9 (7.4)	\bullet 45.9 (6.8)
yes	FBCSP+DSS+LDA	77.1 (8.4)	56.4 (5.3)	\bullet 47.1 (7.4)	48.4 (9.0)
	URPA+MDM	70.8 (8.2)	\bullet 46.6 (7.2)	51.4 (3.7)	48.4 (6.1)
	SPDOT+TSM+SVM	\bullet 63.0 (9.2)	\bullet 45.9 (6.0)	\bullet 42.0 (4.7)	\bullet 40.4 (7.5)
	EEGNet+DANN	\bullet 49.8 (3.7)	\bullet 49.3 (6.7)	\bullet 49.4 (6.8)	50.0 (7.3)
	ShConvNet+DANN	\bullet 57.5 (7.6)	\bullet 54.0 (5.1)	51.5 (4.9)	48.8 (5.7)
	<i>TSMNet(SPDDSMBN)</i>	77.7 (10.0)	57.8 (5.8)	54.7 (7.3)	52.4 (8.8)